Nanoscale Horizons

ROYAL SOCIETY OF CHEMISTRY

COMMUNICATION

View Article Online
View Journal | View Issue

Cite this: *Nanoscale Horiz.*, 2025, **10**, 1405

Received 28th February 2025,
Accepted 1st May 2025

DOI: 10.1039/d5nh00117j

rsc.li/nanoscale-horizons

Graphene oxide/DNA-aerogel pressure and acoustic sensor†

Siyu Chen, [ab] Pengxiang Zhang, [ab] Jinpei Zhao,[a] Kostya S. Novoselov[ab] and Daria V. Andreeva *[ab]

The increasing demand for health monitoring, voice detection, electronic skins, and human–computer interaction has accelerated the development of highly sensitive, flexible, and miniaturized pressure and acoustic sensors. Among various sensing technologies, piezoresistive sensors offer advantages such as simple fabrication, low power consumption, and broad detection ranges, making them well-suited for detecting subtle vibrations and acoustic signals. However, traditional piezoresistive materials, including metals and semiconductors, are inherently stiff and brittle, limiting their integration into wearable electronics and bio-integrated devices. To overcome these challenges, we introduce a graphene oxide (GO)/deoxyribonucleic acid (DNA) aerogel, synthesized *via* a self-assembly approach using pre-formed hydrogel membranes. This biodegradable and biocompatible aerogel features tunable pore sizes, low density, and excellent mechanical resilience. Upon reduction, the GO/DNA aerogel exhibits high piezoresistive sensitivity (1.74 kPa^{-1}) in the low-pressure range (0–130 Pa), surpassing conventional pressure sensors. Additionally, it detects acoustic signals, achieving a sensitivity of 74.4 kPa^{-1}, outperforming existing acoustic sensors. These findings highlight the potential of rGO/DNA aerogels as materials for next-generation wearable electronics, biomedical diagnostics, and soft robotics.

New concepts

The development of flexible, high-sensitivity pressure and acoustic sensors is crucial for advancing wearable electronics, biomedical diagnostics, and human–computer interaction. However, existing piezoresistive sensors rely on rigid materials, limiting their adaptability and biocompatibility. In this work, we introduce a graphene oxide (GO)/deoxyribonucleic acid (DNA) aerogel, synthesized through a novel self-assembly approach using pre-formed hydrogel membranes. This design enables precise pore size tuning, resulting in a low-density, biodegradable, and biocompatible sensor material with good mechanical stability. The aerogel's porous architecture allows for efficient conductive pathway modulation under external stimuli, leading to a high pressure sensitivity of 1.74 kPa^{-1} in the low-pressure range (0–130 Pa) and acoustic sensitivity of 74.4 kPa^{-1}, outperforming conventional sensors. By combining GO and DNA, this work establishes a new paradigm for sustainable, bio-integrated sensor technologies with applications in soft robotics, health monitoring, and next-generation AI-driven interfaces.

Introduction

The increasing demand for health monitoring, voice detection, electronic skins, and human–computer interaction has driven significant advancements in the development of innovative building blocks for miniature sensors in recent years.[1–5] The ability to detect subtle vibrations through pressure and acoustic sensors is critical for advancing artificial intelligence technologies. Among various sensor types, piezoresistive sensors stand out due to their simple fabrication process, low power consumption, broad detection range, and ease of signal acquisition.[6,7] The piezoresistive effect also allows nanomaterial-based pressure sensors to detect and respond to sound, which propagates as mechanical waves involving both pressure and displacement.[8,9] When subjected to sound wave-induced variations, piezoresistive materials undergo resistance changes, enabling the precise capture of subtle acoustic signals. This capability makes them highly valuable for applications such as environmental noise monitoring and advanced diagnostic tools in medical and industrial settings.[10–12]

Intrinsic piezoresistive materials, such as metals and semiconductors, are inherently stiff and brittle, making their integration into wearable electronics challenging.[13] Their inherent mechanical properties hinder the flexibility and durability needed for seamless, long-term integration into flexible devices. Moreover, integrating these materials into miniature devices involves complex fabrication processes. As an alternative, graphene-based aerogels with porous structures have emerged as a feasible design for the piezoresistive pressure sensor due to their high sensitivity, large strain range, good pressure tolerance, and wide detection range.[14] In graphene-based composites,[15–17] the change of the conductive

[a] *Institute for Functional Intelligent Materials, National University of Singapore, 117544, Singapore. E-mail: daria@nus.edu.sg*
[b] *Department of Materials Science and Engineering, National University of Singapore, 117575, Singapore*

† Electronic supplementary information (ESI) available. See DOI: https://doi.org/10.1039/d5nh00117j

pathway and areas are responsible for the alteration of resistance in response to the external stimulus.[2,18]

In this study, a self-assembly approach based on the preformation of a 2D hydrogel membrane[19] is introduced to fabricate a porous composite[20] for pressure and acoustic sensor applications, using graphene oxide (GO) and deoxyribonucleic acid (DNA) as precursors. The resulting GO/DNA aerogel features tunable pore size, light density, and mechanical robustness. After reduction, the reduced graphene oxide (rGO)/DNA aerogel serves as the sensing material for constructing both pressure and acoustic sensors.

Diverse approaches, including template-directed,[21,22] self-assembly,[23–25] electrospinning,[26–28] and 3D printing,[29–31] have been used for the fabrication of sensors. The structural adaptability and chemical versatility of GO[32,33] make it highly compatible with these methods, enabling the design of biomedical devices.[7] Despite being a biodegradable macromolecular compound derived from renewable sources, DNA is rarely utilized as an effective structural component in biomedical devices. However, it has been demonstrated that self-assembly *via* π–π stacking and hydrogen bonding between GO and DNA facilitates the formation of a 2D composite membrane, integrating the advantages of both materials.[19,20] The controlled swelling of DNA between GO layers enables precise tuning of the pore size, while the rigid GO sheets provide structural integrity, ensuring stability and durability in the device.

Compressive and fatigue tests were conducted to investigate the sensitivity and durability of the sensor. The sensitivity reaches 1.74 kPa^{-1} within the low-pressure range of 0–130 Pa, which is higher than the typical values reported from other pressure sensors.[34–56] It also exhibited a broad detection range up to 160 kPa. The rGO/DNA aerogel also demonstrated excellent sound detection capability with the highest sensitivity of 74.4 kPa^{-1}, a wide frequency response range of 300–4000 Hz, and a relatively low sound pressure detection limit of 68 dB, which is comparable to or even superior than those of previously reported acoustic sensors.[41,57–63]

Results and discussion

The self-assembly of the GO/DNA hydrogel membrane, composed of lamellar DNA-encapsulated GO sheets (Fig. 1a), is described in ref. 19. Briefly, the π–π stacking between sp^2-hybridized domains of GO and DNA bases drive the formation of DNA multilayers within the GO layers. When immersed in water, the hydrophilic DNA swells within the interlayer spacing of GO to achieve the equilibrium swelling ratio of 145 g g^{-1} and GO layers act as the supporting platform. The immersion time in water was controlled at 2, 4, 6, 8, and 10 minutes, respectively, resulting in tunable pore length, weight density, and porosity of the GO/DNA aerogels. The SEM images (Fig. 1b–f) confirm the formation of a porous network, with the average pore length increasing from 10 μm to 74 μm as the immersion time increases (Fig. 1g). Correspondingly, the weight density decreased from 73.0 mg cm^{-3} to 14.6 mg cm^{-3}, while the porosity increased from 94.6% to 99.0% (Fig. 1h). The Young's modulus of the composite aerogels also decreased from 2.75 kPa to 0.92 kPa with increasing pore length (Fig. 1i). Notably, these values remain significantly higher than that of pure GO aerogels (0.38 kPa), owing to the hydrogen bonding cross-linking interactions between GO and DNA. This structural tunability, enabled by a simple and controllable swelling process, offers a versatile platform for tailoring the mechanical properties and potential sensing performance of the aerogels to meet specific application requirements.

The successful introduction of DNA molecules into the GO layers was confirmed by Fourier-transform infrared (FTIR) spectra (Fig. 1j). The characteristic peaks of DNA appeared for the GO/DNA composite, such as the narrow and intense peaks at 1636 cm^{-1} (–NH–), 1209 cm^{-1} ($(PO_2^-)_{as}$), 1049 ($(PO_2^-)_s$), and 779 cm^{-1} (sugar-phosphate). The peaks at 1373–1537 cm^{-1} correspond to DNA base vibration.[64,65] The composite can be easily shaped and processed into various forms (Fig. S1, ESI†).

After microwave reduction (details provided in the Experimental section of the ESI†), the peak intensities corresponding to oxygen-containing functional groups (C═O at 1786 cm^{-1} and C–OH at 1423 cm^{-1}) and phosphorus-related groups (PO_2^- at 1209 and 1049 cm^{-1} and O–P–O at 966 cm^{-1}) significantly decreased (Fig. 2a). This transformation is likely due to arc evolution and carbonization during the reduction process.[9]

Wrinkles were observed on the walls of the voids in the rGO/DNA aerogel, in contrast to the smooth pore surfaces in the GO/DNA aerogel (Fig. 2b). The resulting wrinkled walls increase the contact surface area under external perturbation, potentially enhancing the aerogel's detection capabilities.[66]

X-ray photoelectron spectroscopy (XPS) provides quantitative insights about the species and content of surface chemical bonds on the aerogel. The C/O ratio increases from 2.55 to 3.16 after reduction (Fig. S3, ESI†), indicating a decrease in oxygen-containing functional groups. DNA molecules contribute to carbon species such as C–N and N–C–N (overlapping with C–O), N–C═O (overlapping with C═O), and N–C(═O)–N (overlapping with O–C═O).[67] The C 1s spectrum of the GO/DNA aerogel exhibits two broad peaks that can be deconvoluted into C–C (284.62 eV), C–O/C–N (285.13 eV), C–O–C (286.25 eV), C═O/DNA base (287.11 eV), and O–C═O (288.53 eV) with the carbon atom composition of 32.52%, 10.18%, 24.20%, 25.92% and 7.19%, respectively (Fig. 2c and Table S1, ESI†). In contrast, the C 1s for rGO/DNA aerogel (Fig. 2c) only depicts a broad peak due to the change in the relative content of these bonds. Specifically, the proportion of C–O increased from 10.18% to 14.89%, and O–C═O (carboxyl) rose from 7.19% to 8.79%. Meanwhile, the proportions of C═O (carbonyl) and C–O–C (epoxy) decreased from 25.92% to 18.55% and from 24.20% to 16.87%, respectively. These changes are consistent with the O 1s spectra (Fig. 2d) and FTIR spectra (Fig. S4, ESI†) and are attributed to the reduction process.[68] The XRD patterns (Fig. S5, ESI†) also indicate an interlayer distance of 3.4 Å between reduced GO sheets. Additionally, the N 1s (Fig. 2e) and P 2p (Fig. 2f) spectra confirm the presence of DNA residues on the aerogel surface in both GO/DNA and rGO/DNA.

A schematic of the pressure-sensing test is illustrated in Fig. 3a. The 3D porous structure of the rGO/DNA aerogel

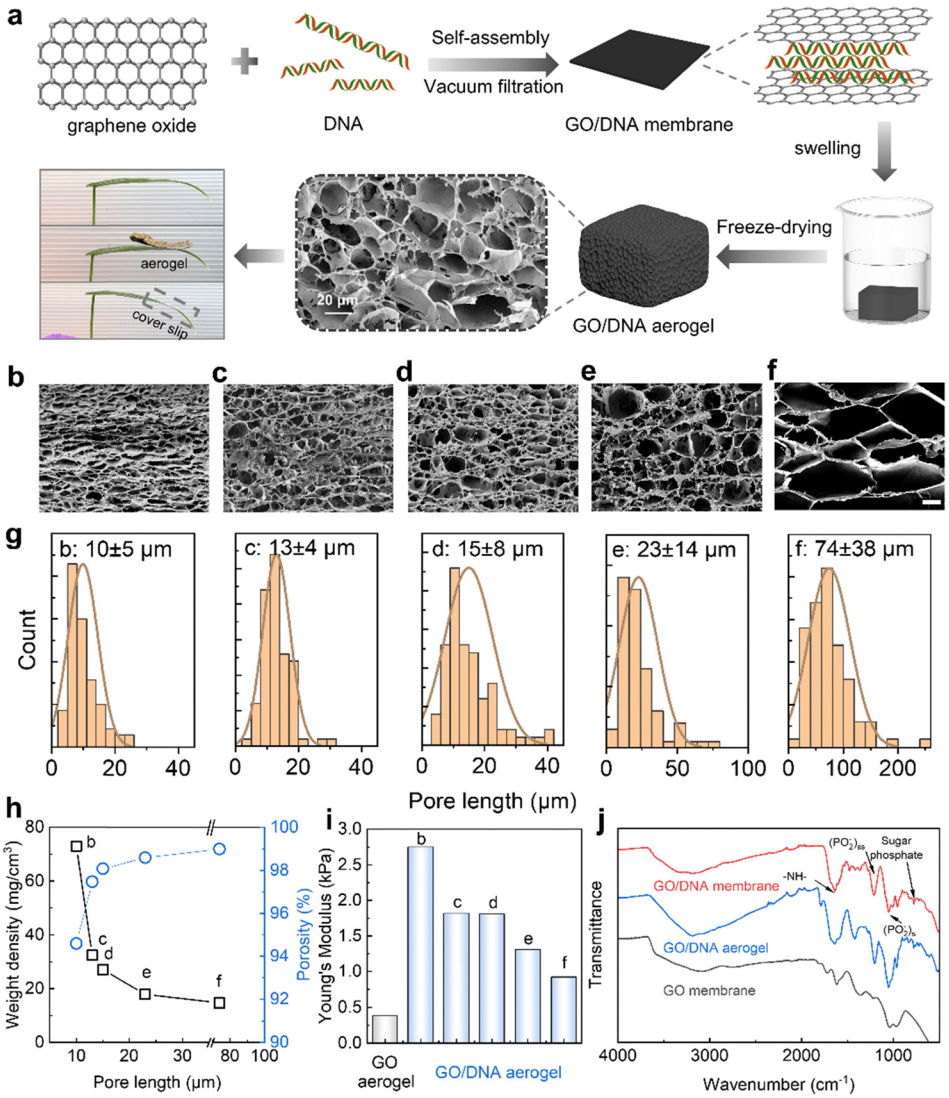

Fig. 1 (a) Schematic illustration of the fabrication process for 3D GO/DNA aerogels from a 2D hydrogel membrane. (b)–(f) SEM images of GO/DNA aerogels with swelling times of 2 min, 4 min, 6 min, 8 min, and 10 min, respectively. Scale bar: 20 μm. (g) Pore size distribution of GO/DNA aerogels in (b)–(f) calculated using ImageJ software. (h) Weight density and porosity of GO/DNA aerogels in (b)–(f) *vs.* pore length. (i) Young's modulus of GO and GO/DNA aerogels in (b)–(f). (j) Fourier-transform infrared spectra of the GO membrane, GO/DNA membrane, and GO/DNA aerogel.

ensures its sensitivity to external pressure.[69] When pressure is applied, pore deformation alters the conductive pathways, thereby changing the resistance of the aerogel. To prevent irreversible collapse and enhance stability, the pressure sensor was encapsulated in elastic polydimethylsiloxane (PDMS), providing additional protection and durability. As shown in Fig. S6 (ESI†), the resistance change of the pressure sensor increases with increasing pore length. Therefore, the rGO/DNA aerogel with a pore size of 74 μm was selected to further study its pressure sensing performance.

The sensitivity (S) of the pressure sensor was calculated using the formula $S = \partial(\Delta R/R_0)/\partial P$, where ΔR represents the change in resistance under loading, R_0 is the initial resistance of the aerogel without loading, and ∂P is the change in applied pressure. The sensitivity values, derived from the slopes in the low-pressure (Fig. 3b) and high-pressure (Fig. 3c) ranges, were determined as follows: 1.74 kPa^{-1} for 0–0.13 kPa, 0.25 kPa^{-1} for 0.13–1 kPa, 0.0167 kPa^{-1} for 2–30 kPa, and 0.0008 kPa^{-1} for 30–160 kPa, respectively. Additionally, the rGO/DNA-aerogel-based pressure sensor detected stimuli as low as 0.31 Pa and maintained a high sensitivity of 1.74 kPa^{-1} within the range of 0–0.13 kPa without PDMS encapsulation. The pressure sensor exhibits a fast response and recovery time of 135 ms, as shown in Fig. 3d. In addition to response speed, it is crucial for sensors to maintain sensitivity under dynamic pressure stimuli at varying frequencies, which are common in real-world application scenarios. An external pressure of 15.6 kPa was applied at frequencies ranging from 0.05 Hz to 1 Hz, as shown in Fig. 3e. The sensor maintained excellent frequency stability and sensitivity even at a high frequency of 1 Hz, which is attributed to the rapid response characteristics of our aerogel. Furthermore, the sensor demonstrated outstanding operational durability, showing stable and

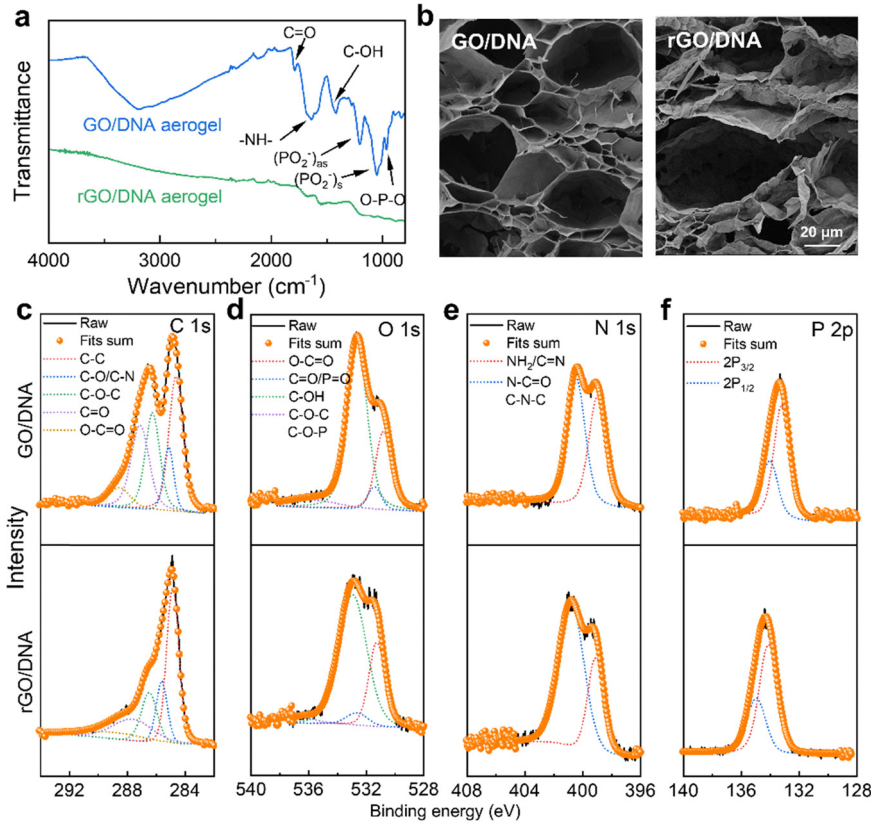

Fig. 2 (a) Fourier-transform Infrared spectra of GO/DNA and rGO/DNA aerogels. (b) Scanning electron microscope images of GO/DNA and rGO/DNA aerogels. Typical high-resolution XPS spectra of (c) C 1s, (d) O 1s, (e) N 1s, and (f) P 2p regions of GO/DNA and rGO/DNA aerogels.

consistent response with minimal variation over 500 consecutive compression–release cycles under a constant pressure of 15.6 kPa (Fig. 3f). The long-term stability was also investigated by storing the device under ambient environmental conditions (25 °C, 62% RH) and monitoring its performance over 14 days. As shown in Fig. S7 (ESI†), the sensor exhibited negligible performance degradation, confirming its excellent long-term stability.

The observed resistance change during compression is attributed to the deformation of the aerogel's porous structure. This could facilitate the formation of new conductive pathways due to increased contact area between the rGO layers. As shown in Fig. 3g, the applied compressive force induced out-of-plane deformation, which consequently leads to additional connections between the rGO nanosheets within the pore walls, as highlighted by the orange rectangle. To further elucidate the sensing mechanism, an equivalent circuit model of the rGO/DNA aerogel-based pressure sensor is presented in Fig. 3h. Initially, the total resistance of the sensor is composed of the contact resistance (R_c) and the intrinsic resistance across the porous structure (R_i). Under external compression, increased contact between the rGO layers introduces parallel conductive pathways, represented as parallel resistance (R_p), thereby reducing the overall resistance. This interconnected microporous architecture enables effective transduction of external pressure and could withstand geometric deformation, resulting in excellent sensing performance over a broad pressure range. However, the sensor's sensitivity decreases at higher pressures, which can be attributed to the saturation of pore compression.

These performances highlight the rGO/DNA aerogel's strong potential for practical pressure sensing applications, particularly for the detection and monitoring of human motions. The applicability of our pressure sensor was further demonstrated by monitoring the gripping of three objects with different weights, including a plastic tube, a glass beaker, and a glass bottle (Fig. 3i). These objects with increasing weight induced increased resistance change due to the higher gripping pressure. Compared to previously reported pressure sensors (Fig. 3j and Table S3, ESI†),[40,42–56] the rGO/DNA aerogel sensor shows extraordinary sensitivity of 1.74 kPa^{-1} in the low-pressure regime, a wide sensing range up to 160 kPa maintaining good sensitivity, and a fast response time of 135 ms. Moreover, these aerogels can be fabricated *via* a simple, feasible, and controllable process from swollen membranes, making them highly promising for large-scale practical applications.

In addition to detecting external mechanical pressure, the rGO/DNA aerogel can sense minute air pressure vibrations generated by environmental sounds. To evaluate its real-time response to audio signals, an rGO/DNA-aerogel-based sound detector was placed beneath a loudspeaker and integrated with an electrical connection (Fig. 4a). The resonant frequency at which a material exhibits maximum vibrational response is fundamentally governed by its intrinsic mechanical and structural

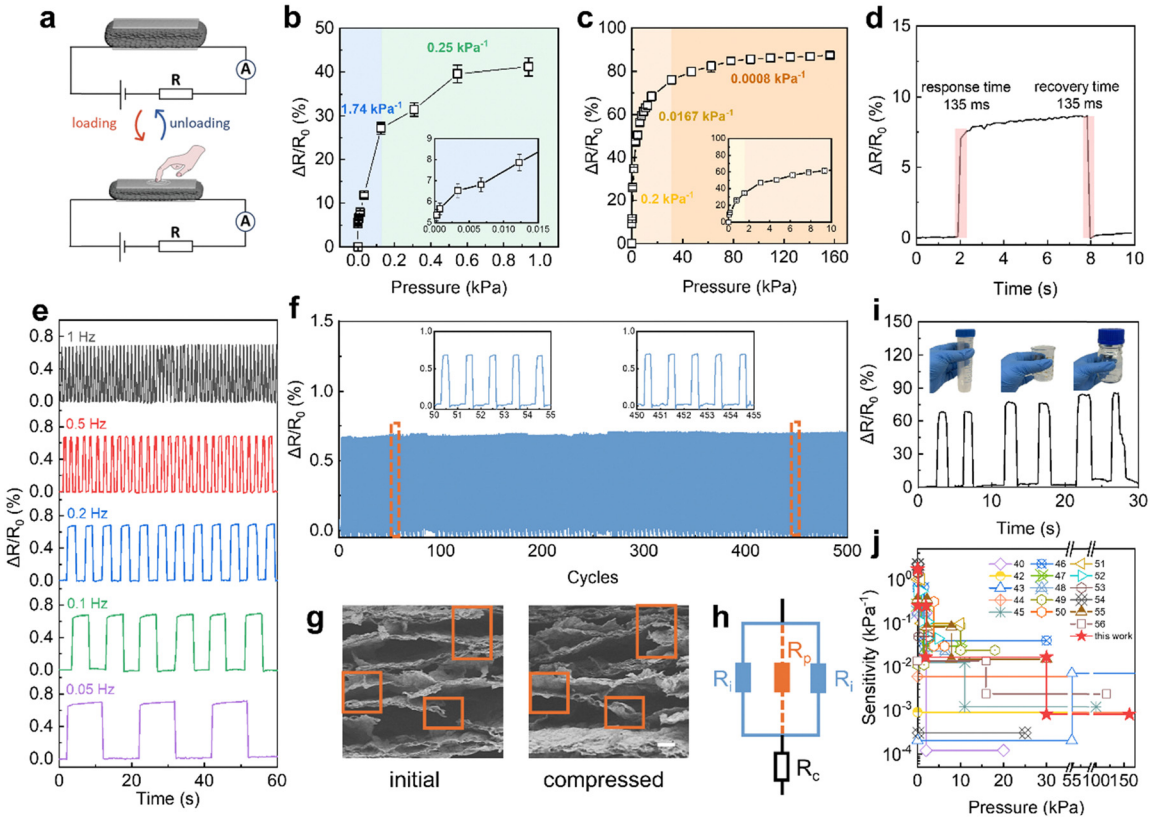

Fig. 3 (a) Schematic of the rGO/DNA aerogel-based pressure sensing test. Resistance response of the rGO/DNA aerogel-based pressure sensor within (b) low-pressure and (c) high-pressure ranges. (d) Response time and recovery time of the pressure sensor. (e) Resistance response to forces at different frequencies. (f) Durability test of the sensor for 500 compress-release cycles under 15.6 kPa. (g) SEM images of the rGO/DNA aerogel before and after compression. Scale bar: 20 μm. (h) Equivalent circuit diagram for the rGO/DNA pressure sensor, where the dotted orange circuit represents the formation of additional conductive pathways under compression. (i) Practical application of the pressure sensor for gripping a plastic tube, glass beaker, and glass bottle. (j) Comparison of sensitivity and pressure detection range in this work with previous works.

properties. In our case of rGO/DNA aerogels, this frequency can be effectively tuned by adjusting key structural parameters such as the porosity (or bulk density), Young's modulus, and geometrical dimensions. The theoretical resonant frequency for a rectangular plate-like structure can be estimated using the following equation:

$$\omega = \sqrt{\frac{Et^2}{12(1-\nu^2)\rho}}\left[\left(\frac{\pi}{a}\right)^2+\left(\frac{\pi}{b}\right)^2\right],$$

where E is the Young's modulus, ν is the Poisson's ratio, ρ is the density, and t, a, and b are the thickness, length, and width of the material, respectively.[70] The calculated resonant frequencies of rGO/DNA aerogels with varying pore length, corresponding to the structures shown in Fig. 1b–f, are presented in Fig. 4b. In addition, the experimentally measured response of aerogel-based acoustic sensors with pore length of 10 μm, 15 μm, and 74 μm at different frequencies were shown as insets. The results indicate that increasing the pore length, which simultaneously increases the thickness and decreases the bulk density, leads to a significant shift in resonant frequency from 325 Hz to 2348 Hz. Considering that the typical human communication range lies between 300 and 3500 Hz, and that the sensor's performance declines dramatically beyond the resonant frequency,[71] aerogels with 74 μm pores were selected for further investigation of their acoustic sensing properties.

Upon exposure to sound, the sensor exhibited significant resistance changes, which correlated with both the frequency and the sound pressure level (SPL) (Fig. 4c). The sensor demonstrated a response frequency range of 300 to 4000 Hz, covering the human communication frequency range (300–3500 Hz). It exhibited higher sensitivity to low- and mid-frequency sound waves, whereas higher frequencies produced minimal pressure variations, insufficient to trigger a significant response. The sensor's minimum activation SPL was 68 dB, equivalent to the sound level of a normal conversation.

The sensitivity (S) of the acoustic sensor was calculated using the equation:[8,72]

$$S = \frac{\Delta R/R_0}{P} = \frac{\Delta V/V_0}{P_0 \times 10^{L_P/20}}$$

where $\Delta V = V - V_0$, with V and V_0 representing the sensor's voltage before and after sound application, respectively. P_0 is the reference sound pressure (2×10^{-5} Pa), and L_p is the SPL in decibels. The sensor's calculated sensitivity across different frequencies ranged from 0.84 kPa^{-1} to 74.4 kPa^{-1}. Compared with other acoustic sensors,[41,57–63] the rGO/DNA aerogel exhibits

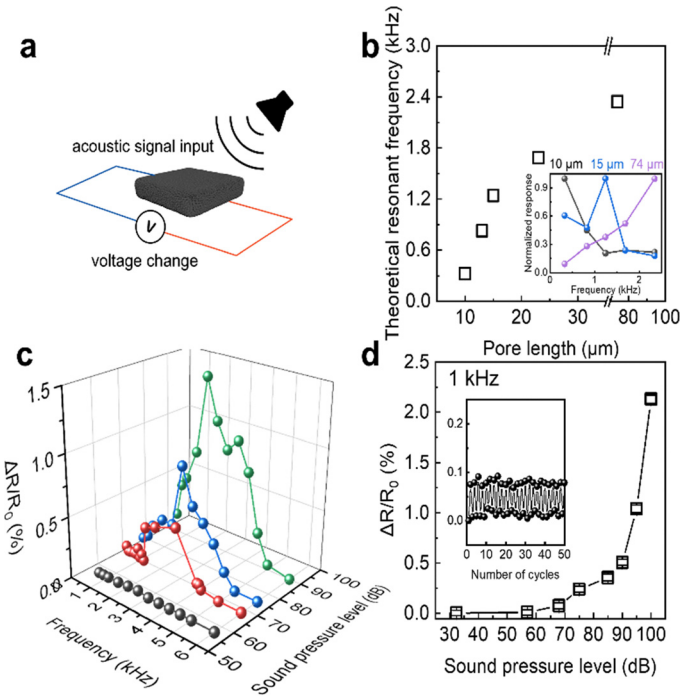

Fig. 4 (a) Schematic of the rGO/DNA aerogel-based acoustic sensing test. (b) Theoretical resonant frequency of rGO/DNA aerogels with different pore lengths. Inset: Normalized response of rGO/DNA aerogel-based acoustic sensors with pore sizes of 10 μm, 15 μm, and 74 μm. (c) Resistance response for different frequencies and sound pressure levels. (d) Resistance response at 1 kHz *vs.* sound pressure level. Inset: Repeatability test at 1 kHz under 50 cycles.

a well-balanced performance for daily communication monitoring with both an appropriate frequency response range (300–4000 Hz) and a relatively low sound pressure detection limit (68 dB). A detailed comparison of key parameters for acoustic sensors is provided in Table S4 (ESI†).

Fig. 4d shows the effect of SPL on the resistance change at 1 kHz. The relative resistance change increased from 0.0093% to 0.51% as the SPL rose from 57 dB to 90 dB. Beyond 90 dB, the resistance change increased sharply, indicating that higher sound intensities enhanced the acoustic output, leading to

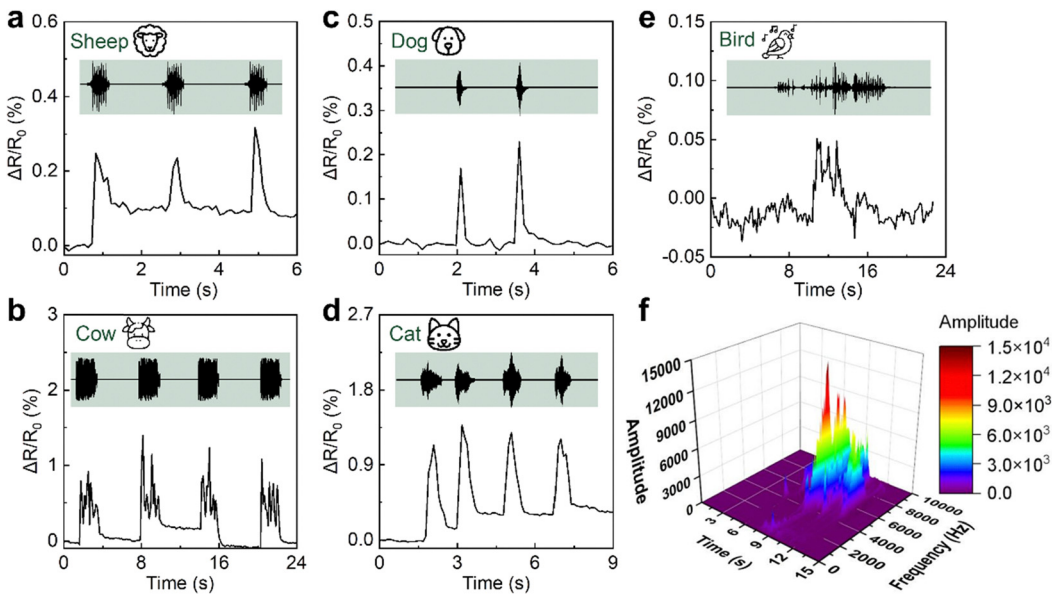

Fig. 5 Resistance response of the rGO/DNA aerogel-based acoustic sensor in response to the audio signals of animal sounds: (a) a sheep, (b) a cow, (c) a dog, (d) a cat, and (e) a bird. (f) The short-time Fourier transform analysis of the bird's chirp.

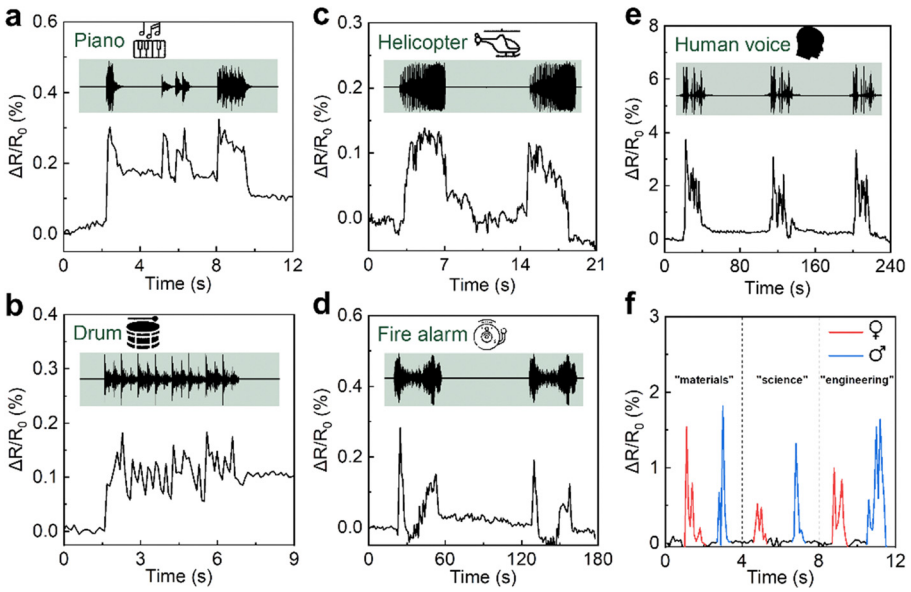

Fig. 6 Resistance response of the rGO/DNA aerogel-based acoustic sensor in response to the audio signals of a (a) piano, (b) drum, (c) helicopter, (d) fire alarm, and (e) human voice. (f) Sensitivity comparison between the words of ''materials'', ''science'', and ''engineering'' from a male and a female tester.

greater pressure variations and more pronounced resistance changes. The inset in Fig. 4d illustrates the consistent resistance change profile of the sensor when exposed to a sound of 1 kHz and 68 dB over 50 cycles, confirming its repeatability in detecting acoustic vibrations.

To explore its potential for miniature devices, we fabricated the rGO/DNA aerogel into a smaller size (3 mm × 3 mm). This miniaturized sensor exhibited an enhanced response of 4.8% at a SPL of 72 dB and 1 kHz (Fig. S8, ESI†).

Thus, these functional materials with a facile fabrication approach, ultralight weight, and flexibility can be further combined with cutting-edge integrated processes and promote their miniaturization and seamless integration within circuits. It was reported that the noise generated by diesel trucks, large air compressors, and a jet taking off could discretely reach 87 dB, 100 dB, and 125 dB, which was intolerable and caused irretrievable damage to hearing.[73] The strong resistance response of the rGO/DNA aerogel sensor to high SPL noise highlights its potential as an effective noise monitoring device.

The ability to distinguish different acoustic signals composed of various frequencies is critical for an acoustic sensor. To evaluate this capability, diverse audio signals including animal sounds (sheep, cow, dog, cat, and bird), and a piano, drum, helicopter, fire alarm, and human voice were tested (Fig. 5 and 6). The sensor's responses were synchronous with the original audio signals, as visualized in their respective waveforms.

The porous structure of the sensor facilitates its high sensitivity to weak acoustic vibrations, resulting in measurable resistance changes. Notably, the resistance change for the cow's moo (Fig. 5b) was significantly more intense and distinct than that for the bird's chirp (Fig. 5e). This disparity arises from differences in the frequency and loudness of the audio signals.

Short-time Fourier transform (STFT) analysis (Fig. 5f and Fig. S9, ESI†) revealed that a cow's moo falls within the 250–1750 Hz range, which is well within the sensor's detectable frequency range (<4000 Hz). The bird's chirp, with a frequency range of 5000–9000 Hz, exceeded the sensor's detection capability. Additionally, the cow's moo exhibited a higher loudness than the bird's chirp, resulting in a greater resistance change and higher sensitivity.

Fig. 6a–d demonstrates that the sensor captured fine details of the pulse waveforms for various audio signals, confirming its applicability as a sound detector. To further validate its feasibility for human–computer interaction, a long sentence spoken by a human voice was repeated three times. The response curve (Fig. 6e) closely matched the spectrogram of the sentence and showed excellent reproducibility across repetitions. Furthermore, distinct words such as ''materials'', ''science'', and ''engineering'' were pronounced by both male and female testers *via* loudspeaker. The sensor's responses (Fig. 6f) displayed distinguishable patterns for different words, likely due to variations in syllable length and duration. Additionally, responses differed between genders, influenced by the frequency and loudness of the voice. Individual variations in pronunciation led to differing sensor responses for the same word. The rGO/DNA aerogel-based sensor's sensitive response to human voices further highlights its potential for voice recognition applications.

Conclusions

In summary, robust 3D GO/DNA and rGO/DNA aerogels were fabricated *via* self-assembly of 2D GO/DNA hydrogel membranes. The resulting GO/DNA aerogels demonstrated an enhanced mechanical strength with Young's modulus of 0.92 kPa to 2.75 kPa, significantly higher than that of the GO aerogel, while maintaining an ultralight density of 14.6 mg cm^{-3} to 73.0 mg cm^{-3}.

Two types of sensors based on the rGO/DNA aerogel were developed to explore its potential applications: pressure sensor

and acoustic sensor. The pressure sensor leveraged the deformable conductive pathways formed by the aerogel's interconnected pore walls, exhibiting excellent sensitivity and repeatability under external forces. It demonstrated responsiveness to minimal stimuli as low as 0.13 kPa, with a high sensitivity of 1.74 kPa^{-1}. The acoustic sensor showed outstanding performance in sound detection, with a broad working frequency range (300–4000 Hz) and notable sensitivity (74.4 kPa^{-1}). Its responses were highly synchronized with audio signals, including animal sounds, human voices, and environmental noise.

The facile fabrication process, straightforward working principles, and high sensitivity of these sensors not only enable miniaturization for enhanced portability and compactness, but also facilitate multi-functional integration with advanced technologies. The dual functionality of the rGO/DNA aerogel-based sensor – capable of detecting both mechanical pressure and acoustic signals – demonstrates its versatility for applications in electronic touchpads, soft robotics, noise monitoring, sound detection, and human–computer interaction.

Author contributions

D. V. A. and K. S. N. designed the experiments and supervised the project. S. C., P. Z., R. L., and J. Z. carried out the experiments and analyzed the experimental results. S. C. and P. Z. co-wrote the paper, and D. V. A. and K. S. N revised the manuscript. S. C. and P. Z. contributed equally to this work. All authors discussed the results and commented on the manuscript.

Data availability

The data supporting this article have been included as part of the ESI† and can be found in the online version.

Conflicts of interest

There are no conflicts to declare.

Acknowledgements

This research is supported by the Ministry of Education, Singapore, under its Research Centre of Excellence award to the Institute for Functional Intelligent Materials (I-FIM, project no. EDUNC-33-18-279-V12).

References

1 J. Park, Y. Lee, J. Hong, M. Ha, Y.-D. Jung, H. Lim, S. Y. Kim and H. Ko, *ACS Nano*, 2014, **8**, 4689–4697.
2 Y. Zang, F. Zhang, C.-A. Di and D. Zhu, *Mater. Horiz.*, 2015, **2**, 140–156.
3 Y. Khan, A. E. Ostfeld, C. M. Lochner, A. Pierre and A. C. Arias, *Adv. Mater.*, 2016, **28**, 4373–4395.
4 K. Yang, Q. Wang, K. S. Novoselov and D. V. Andreeva, *Nanoscale Horiz.*, 2023, **8**, 1243–1252.
5 J. H. Bong, S. Grebenchuk, K. G. Nikolaev, C. P. T. Chee, K. Yang, S. Chen, D. Baranov, C. R. Woods, D. V. Andreeva and K. S. Novoselov, *Nanoscale Horiz.*, 2024, **9**, 863–872.
6 T. Q. Trung and N. E. Lee, *Adv. Mater.*, 2016, **28**, 4338–4372.
7 M. Cao, J. Su, S. Fan, H. Qiu, D. Su and L. Li, *Chem. Eng. J.*, 2021, **406**, 126777.
8 S. Gong, L. W. Yap, Y. Zhu, B. Zhu, Y. Wang, Y. Ling, Y. Zhao, T. An, Y. Lu and W. Cheng, *Adv. Funct. Mater.*, 2020, **30**, 1910717.
9 L. Q. Tao, H. Tian, Y. Liu, Z. Y. Ju, Y. Pang, Y. Q. Chen, D. Y. Wang, X. G. Tian, J. C. Yan, N. Q. Deng, Y. Yang and T. L. Ren, *Nat. Commun.*, 2017, **8**, 14579.
10 M. Alghrairi, B. A. K. Farhan, H. M. Ridha, S. Mutashar, W. Algriree and B. M. Sabbar, *J. Phys. Commun.*, 2024, **8**, 092001.
11 Z. Lin, S. Duan, M. Liu, C. Dang, S. Qian, L. Zhang, H. Wang, W. Yan and M. Zhu, *Adv. Mater.*, 2024, **36**, 2306880.
12 T. Su, N. Liu, D. Lei, L. Wang, Z. Ren, Q. Zhang, J. Su, Z. Zhang and Y. Gao, *ACS Nano*, 2022, **16**, 8461–8471.
13 X. Jiang, Z. Ren, Y. Fu, Y. Liu, R. Zou, G. Ji, H. Ning, Y. Li, J. Wen, H. J. Qi, C. Xu, S. Fu, J. Qiu and N. Hu, *ACS Appl. Mater. Interfaces*, 2019, **11**, 37051–37059.
14 Y. Ding, T. Xu, O. Onyilagha, H. Fong and Z. Zhu, *ACS Appl. Mater. Interfaces*, 2019, **11**, 6685–6704.
15 M. Lin, M. Trubianov, K. Yang, S. Chen, Q. Wang, J. Wu, X. Liao, A. Greiner, K. S. Novoselov and D. V. Andreeva, *Sci. Technol. Adv. Mater.*, 2024, **25**, 2421757.
16 K. Yang, K. G. Nikolaev, X. Li, I. Erofeev, U. M. Mirsaidov, V. G. Kravets, A. N. Grigorenko, X. Qiu, S. Zhang, K. S. Novoselov and D. V. Andreeva, *Adv. Sci.*, 2025, **12**, 2408533.
17 K. Yang, K. G. Nikolaev, X. Li, A. Ivanov, J. H. Bong, I. Erofeev, U. M. Mirsaidov, V. G. Kravets, A. N. Grigorenko, S. Zhang, X. Qiu, K. S. Novoselov and D. V. Andreeva, *Proc. Natl. Acad. Sci. U. S. A.*, 2024, **121**, e2414449121.
18 T. Xu, Y. Ding, Z. Wang, Y. Zhao, W. Wu, H. Fong and Z. Zhu, *J. Mater. Chem. C*, 2017, **5**, 10288–10294.
19 S. Chen, C. J. M. Lee, G. S. X. Tan, P. R. Ng, P. Zhang, J. Zhao, K. S. Novoselov and D. V. Andreeva, *Macromol. Rapid Commun.*, 2025, **46**, 2400518.
20 X. Leng, S. Chen, S. R. McCuskey, Y. Zhang, S. J. W. Chan, G. Quek, M. C. F. Costa, P. Zhang, J. Wu, K. G. Nikolaev, G. C. Bazan, K. S. Novoselov and D. V. Andreeva, *Adv. Electron. Mater.*, 2024, **10**, 2400137.
21 H. Liu, M. Dong, W. Huang, J. Gao, K. Dai, J. Guo, G. Zheng, C. Liu, C. Shen and Z. Guo, *J. Mater. Chem. C*, 2017, **5**, 73–83.
22 Y. A. Samad, Y. Li, A. Schiffer, S. M. Alhassan and K. Liao, *Small*, 2015, **11**, 2380–2385.
23 Y. Xu, K. Sheng, C. Li and G. Shi, *ACS Nano*, 2010, **4**, 4324–4330.
24 M. A. Worsley, S. O. Kucheyev, H. E. Mason, M. D. Merrill, B. P. Mayer, J. Lewicki, C. A. Valdez, M. E. Suss, M. Stadermann and P. J. Pauzauskie, *Chem. Commun.*, 2012, **48**, 8428–8430.
25 W. Lv, Y. Tao, W. Ni, Z. Zhou, F.-Y. Su, X.-C. Chen, F.-M. Jin and Q.-H. Yang, *J. Mater. Chem.*, 2011, **21**, 12352–12357.
26 L. Haghighi Poudeh, D. Cakiroglu, F. Ç. Cebeci, M. Yildiz, Y. Z. Menceloglu and B. Saner Okan, *ACS Omega*, 2018, **3**, 6400–6410.

27 S. Nagarajan, C. Pochat-Bohatier, C. Teyssier, S. Balme, P. Miele, N. Kalkura, V. Cavaillès and M. Bechelany, *RSC Adv.*, 2016, **6**, 109150.
28 Y. J. Yun, W. G. Hong, N.-J. Choi, H. J. Park, S. E. Moon, B. H. Kim, K.-B. Song, Y. Jun and H.-K. Lee, *Nanoscale*, 2014, **6**, 6511–6514.
29 F. Wang, Y. Jiang, Y. Liu, F. Guo, W. Fang, Z. Xu and C. Gao, *Carbon*, 2020, **159**, 166–174.
30 Q. Zhang, F. Zhang, S. P. Medarametla, H. Li, C. Zhou and D. Lin, *Small*, 2016, **12**, 1702–1708.
31 E. García-Tuñon, S. Barg, J. Franco, R. Bell, S. Eslava, E. D'Elia, R. C. Maher, F. Guitian and E. Saiz, *Adv. Mater.*, 2015, **27**, 1688–1693.
32 H. Kim and J.-H. Ahn, *Carbon*, 2017, **120**, 244–257.
33 H. Chen, F. Zhuo, J. Zhou, Y. Liu, J. Zhang, S. Dong, X. Liu, A. Elmarakbi, H. Duan and Y. Fu, *Chem. Eng. J.*, 2023, **464**, 142576.
34 Z. Lin, S. Duan, M. Liu, C. Dang, S. Qian, L. Zhang, H. Wang, W. Yan and M. Zhu, *Adv. Mater.*, 2024, **36**, 2306880.
35 S. C. B. Mannsfeld, B. C. K. Tee, R. M. Stoltenberg, C. V. H. H. Chen, S. Barman, B. V. O. Muir, A. N. Sokolov, C. Reese and Z. Bao, *Nat. Mater.*, 2010, **9**, 859–864.
36 A. D. Smith, F. Niklaus, A. Paussa, S. Vaziri, A. C. Fischer, M. Sterner, F. Forsberg, A. Delin, D. Esseni, P. Palestri, M. Östling and M. C. Lemme, *Nano Lett.*, 2013, **13**, 3237–3242.
37 T. Someya, T. Sekitani, S. Iba, Y. Kato, H. Kawaguchi and T. Sakurai, *Proc. Natl. Acad. Sci. U. S. A.*, 2004, **101**, 9966–9970.
38 H. Tian, Y. Shu, X.-F. Wang, M. A. Mohammad, Z. Bie, Q.-Y. Xie, C. Li, W.-T. Mi, Y. Yang and T.-L. Ren, *Sci. Rep.*, 2015, **5**, 8603.
39 W. Wu, X. Wen and Z. L. Wang, *Science*, 2013, **340**, 952–957.
40 H.-B. Yao, J. Ge, C.-F. Wang, X. Wang, W. Hu, Z.-J. Zheng, Y. Ni and S.-H. Yu, *Adv. Mater.*, 2013, **25**, 6692–6698.
41 S. Gong, W. Schwalb, Y. Wang, Y. Chen, Y. Tang, J. Si, B. Shirinzadeh and W. Cheng, *Nat. Commun.*, 2014, **5**, 3132.
42 L.-Q. Tao, K.-N. Zhang, H. Tian, Y. Liu, D.-Y. Wang, Y.-Q. Chen, Y. Yang and T.-L. Ren, *ACS Nano*, 2017, **11**, 8790–8795.
43 Y. Pang, H. Tian, L. Tao, Y. Li, X. Wang, N. Deng, Y. Yang and T.-L. Ren, *ACS Appl. Mater. Interfaces*, 2016, **8**, 26458–26462.
44 Y. Wei, X. Li, Y. Wang, T. Hirtz, Z. Guo, Y. Qiao, T. Cui, H. Tian, Y. Yang and T.-L. Ren, *ACS Nano*, 2021, **15**, 17738–17747.
45 H. Liu, H. Xiang, Y. Wang, Z. Li, L. Qian, P. Li, Y. Ma, H. Zhou and W. Huang, *ACS Appl. Mater. Interfaces*, 2019, **11**, 40613–40619.
46 N. Yang, H. Liu, X. Yin, F. Wang, X. Yan, X. Zhang and T. Cheng, *ACS Appl. Mater. Interfaces*, 2022, **14**, 45978–45987.
47 L. Zhao, F. Qiang, S.-W. Dai, S.-C. Shen, Y.-Z. Huang, N.-J. Huang, G.-D. Zhang, L.-Z. Guan, J.-F. Gao, Y.-H. Song and L.-C. Tang, *Nanoscale*, 2019, **11**, 10229–10238.
48 Y. Qin, Q. Peng, Y. Ding, Z. Lin, C. Wang, Y. Li, F. Xu, J. Li, Y. Yuan, X. He and Y. Li, *ACS Nano*, 2015, **9**, 8933–8941.
49 Y. Xiong, Y. Zhu, X. Liu, P. Zhu, Y. Hu, R. Sun and C.-P. Wong, *Mater. Today Commun.*, 2020, **24**, 100970.
50 C. Mu, Y. Song, W. Huang, A. Ran, R. Sun, W. Xie and H. Zhang, *Adv. Funct. Mater.*, 2018, **28**, 1707503.
51 L. Shi, Z. Li, M. Chen, Y. Qin, Y. Jiang and L. Wu, *Nat. Commun.*, 2020, **11**, 3529.
52 C. Cai, H. Gong, W. Li, F. Gao, Q. Jiang, Z. Cheng, Z. Han and S. Li, *RSC Adv.*, 2021, **11**, 13898–13905.
53 Z. Han, Z. Cheng, Y. Chen, B. Li, Z. Liang, H. Li, Y. Ma and X. Feng, *Nanoscale*, 2019, **11**, 5942–5950.
54 X. Zhang, F. Chen, L. Han, G. Zhang, Y. Hu, W. Jiang, P. Zhu, R. Sun and C.-P. Wong, *Adv. Eng. Mater.*, 2021, **23**, 2000902.
55 S. Xu, X. Li, G. Sui, R. Du, Q. Zhang and Q. Fu, *Chem. Eng. J.*, 2020, **381**, 122666.
56 F. He, X. You, H. Gong, Y. Yang, T. Bai, W. Wang, W. Guo, X. Liu and M. Ye, *ACS Appl. Mater. Interfaces*, 2020, **12**, 6442–6450.
57 S. Gong, L. W. Yap, Y. Zhu, B. Zhu, Y. Wang, Y. Ling, Y. Zhao, T. An, Y. Lu and W. Cheng, *Adv. Funct. Mater.*, 2020, **30**, 1910717.
58 I. Graz, M. Kaltenbrunner, C. Keplinger, R. Schwödiauer, S. Bauer, S. P. Lacour and S. Wagner, *Appl. Phys. Lett.*, 2006, 89.
59 L.-Q. Tao, H. Tian, Y. Liu, Z.-Y. Ju, Y. Pang, Y.-Q. Chen, D.-Y. Wang, X.-G. Tian, J.-C. Yan, N.-Q. Deng, Y. Yang and T.-L. Ren, *Nat. Commun.*, 2017, **8**, 14579.
60 Y. Jin, B. Wen, Z. Gu, X. Jiang, X. Shu, Z. Zeng, Y. Zhang, Z. Guo, Y. Chen, T. Zheng, Y. Yue, H. Zhang and H. Ding, *Adv. Mater. Technol.*, 2020, **5**, 2000262.
61 Y. Okamoto, T.-V. Nguyen, H. Takahashi, Y. Takei, H. Okada and M. Ichiki, *Sci. Rep.*, 2023, **13**, 6503.
62 C. Lang, J. Fang, H. Shao, X. Ding and T. Lin, *Nat. Commun.*, 2016, **7**, 11108.
63 S. Gong, X. Zhang, X. A. Nguyen, Q. Shi, F. Lin, S. Chauhan, Z. Ge and W. Cheng, *Nat. Nanotechnol.*, 2023, **18**, 889–897.
64 K. Serec, S. D. Babić, R. Podgornik and S. Tomić, *Nucleic Acids Res.*, 2016, **44**, 8456–8464.
65 M. L. S. Mello and B. C. Vidal, *PLoS One*, 2012, **7**, e43169.
66 C. Liu, H. Li, J. Zhao, J. Zhu, X. Huan, Y. Zhang, K. Xu, H. Geng, X. Chen, W. Ding, L. Zu, L. Ge, X. Jia, Q. Meng and X. Yang, *Chem. Eng. J.*, 2024, **494**, 153140.
67 A. J. Patil, J. L. Vickery, T. B. Scott and S. Mann, *Adv. Mater.*, 2009, **21**, 3159–3164.
68 L. Stobinski, B. Lesiak, A. Malolepszy, M. Mazurkiewicz, B. Mierzwa, J. Zemek, P. Jiricek and I. Bieloshapka, *J. Electron Spectrosc. Relat. Phenom.*, 2014, **195**, 145–154.
69 M. Cao, J. Su, S. Fan, H. Qiu, D. Su and L. Li, *Chem. Eng. J.*, 2021, **406**, 126777.
70 J. Suo, Y. Liu, C. Wu, M. Chen, Q. Huang, Y. Liu, K. Yao, Y. Chen, Q. Pan, X. Chang, A. Y. L. Leung, H. Y. Chan, G. Zhang, Z. Yang, W. Daoud, X. Li, V. A. L. Roy, J. Shen, X. Yu, J. Wang and W. J. Li, *Adv. Sci.*, 2022, **9**, e2203565.
71 Y. H. Jung, S. K. Hong, H. S. Wang, J. H. Han, T. X. Pham, H. Park, J. Kim, S. Kang, C. D. Yoo and K. J. Lee, *Adv. Mater.*, 2020, **32**, 1904020.
72 C. Lang, J. Fang, H. Shao, X. Ding and T. Lin, *Nat. Commun.*, 2016, **7**, 1–7.
73 D. F. Anthrop, *Univ. Torr. Law J.*, 1970, **20**, 1–17.